

Constraints on Planetesimal Collision Models in Debris Disks

Meredith A. MacGregor¹, David J. Wilner¹, Claire Chandler², Luca Ricci¹, Sarah T. Maddison³, Steven R. Cranmer⁴, Sean M. Andrews¹, A. Meredith Hughes⁵, Amy Steele⁶

ABSTRACT

Observations of debris disks offer a window into the physical and dynamical properties of planetesimals in extrasolar systems through the size distribution of dust grains. In particular, the millimeter spectral index of thermal dust emission encodes information on the grain size distribution. We have made new VLA observations of a sample of seven nearby debris disks at 9 mm, with 3'' resolution and $\sim 5 \mu\text{Jy}/\text{beam}$ rms. We combine these with archival ATCA observations of eight additional debris disks observed at 7 mm, together with up-to-date observations of all disks at (sub)millimeter wavelengths from the literature to place tight constraints on the millimeter spectral indices and thus grain size distributions. The analysis gives a weighted mean for the slope of the power law grain size distribution, $n(a) \propto a^{-q}$, of $\langle q \rangle = 3.36 \pm 0.02$, with a possible trend of decreasing q for later spectral type stars. We compare our results to a range of theoretical models of collisional cascades, from the standard self-similar, steady-state size distribution ($q = 3.5$) to solutions that incorporate more realistic physics such as alternative velocity distributions and material strengths, the possibility of a cutoff at small dust sizes from radiation pressure, as well as results from detailed dynamical calculations of specific disks. Such effects can lead to size distributions consistent with the data, and plausibly the observed scatter in spectral indices. For the AU Mic system, the VLA observations show clear evidence of a highly

¹Harvard-Smithsonian Center for Astrophysics, 60 Garden Street, Cambridge, MA 02138, USA

²National Radio Astronomy Observatory, Socorro, NM 87801, USA

³Centre for Astrophysics & Supercomputing, Swinburne University, Hawthorn, VIC 3122, Australia

⁴Department of Astrophysical and Planetary Sciences, Laboratory for Atmospheric and Space Physics, University of Colorado, Boulder, CO 80309, USA

⁵Department of Astronomy, Van Vleck Observatory, Wesleyan University, Middletown, CT 06459, USA

⁶Department of Astronomy, University of Maryland, College Park, MD 20742, USA

variable stellar emission component; this stellar activity obviates the need to invoke the presence of an asteroid belt to explain the previously reported compact millimeter source in this system.

Subject headings: circumstellar matter — planets and satellites: formation — stars: individual (AU Mic) — submillimeter: planetary systems

1. Introduction

Debris disks represent the end stage of protoplanetary disk evolution. As such, they provide essential information on the processes of planet formation and circumstellar disk dispersion (see reviews by Backman & Paresce 1993; Wyatt 2008; Matthews et al. 2014). The small dust grains detected at optical through centimeter wavelengths are thought to be produced by the collisional erosion of larger bodies, analogous to comets or Kuiper Belt Objects, commonly referred to as planetesimals. These kilometer-sized remnants of planet formation are effectively invisible around other stars, but emission from the dusty debris produced in ongoing collisions offers a unique window into their physical properties and dynamics. In particular, the spectral index of dust emission at millimeter to radio wavelengths encodes information on the grain size distribution within disks that can be used to constrain collisional models of planetesimals (Ricci et al. 2012, 2015b).

The dominant mechanism responsible for stirring the planetesimals within debris disks to incite collisions remains controversial. Stirring could be triggered by the ongoing formation of Pluto-sized bodies within the disk (Kenyon & Bromley 2002, 2008) or by the dynamical effects of fully formed planets (Mustill & Wyatt 2009). In either case, the reference model for dust production is the steady-state collisional cascade first formulated by Dohnanyi (1969). This model assumes that the relative velocities and tensile strengths of the colliding bodies are independent of size, and leads to a power law size distribution, $n(a) \propto a^{-q}$ with index $q = 3.5$. However, the fragmentation process in debris disks could be more complex. Recent analytic and numerical studies relax some of the restrictive assumptions of the reference model, and incorporate more realistic dynamics and material physics. Including a size-dependent velocity distribution predicts a steeper distribution, $q \sim 4$ (Pan & Schlichting 2012; Gáspár et al. 2012), while decreasing the tensile strength of the colliding bodies predicts a shallower distribution, $q \sim 3$ (Pan & Sari 2005).

We present observations of seven debris disks at 9 mm using the Karl G. Jansky Very Large Array (VLA) of the National Radio Astronomy Observatory. These long wavelength observations probe emission from the largest accessible dust grains in the disks. When com-

bined with (sub)millimeter data, these observations provide a long lever arm in wavelength that mitigates the impact of absolute calibration uncertainties on spectral index determinations. In addition, the spectral slopes at these long wavelengths are relatively insensitive to the effects of temperature, given typical debris belts at 10’s of K. We combine this sample with observations of eight additional debris disks with the Australia Telescope Compact Array (ATCA) at 7 mm. By pairing these long wavelength measurements with previous observations at shorter (sub)millimeter wavelengths, we can determine the spectral index of the dust emission and thus the grain size power law index q for the combined sample of fifteen debris disks. We compare our results with predictions from existing collisional cascade models and explore the effects of material strengths, velocity distributions, and small-size cutoffs on the steady-state grain size distribution.

In Section 2 we present the VLA sample of debris disks. Sections 3 and 4 discuss the VLA observations, analysis, and results. In Section 5, we describe how we determine the slope of the grain size distribution, q , and we present the results for the combined VLA and ATCA sample of debris disks. In Section 6, we compare our results to predictions from collisional cascade models and discuss results from analytical modeling of a steady-state grain population. In Section 7, we summarize the main conclusions of this study.

2. VLA Sample

We selected a sample of seven debris disks to observe with the VLA at 9 mm to measure spectral indices and constrain the slope of the grain size distribution, q . The sample was assembled based on the following criteria: 1) accessible source declinations, $\delta > -35^\circ$, 2) evidence in the literature for strong millimeter/submillimeter emission ($F_{0.85\text{mm}} \gtrsim 8 \text{ mJy}$), and 3) small enough angular extent to obtain reliable total flux measurements using the most compact array configurations. Table 1 lists the source positions and stellar properties, and a brief discussion of each target follows. All of these disks have been studied extensively at other wavelengths and have well sampled spectral energy distributions (SEDs) through the far-infrared. In addition, most of these disks have interferometric data that resolve their millimeter emission structure, either from the Submillimeter Array (SMA) or the Atacama Large Millimeter/submillimeter Array (ALMA).

2.1. HD 377

HD 377 is a G2V star at a distance of 39.1 ± 2 pc (van Leeuwen 2007) with an estimated age of ~ 150 Myr (Geers et al. 2012). Spectral energy distribution modeling indicates the presence of dust between 3 and 150 AU (Roccatagliata et al. 2009) and results in a two temperature component fit with a warmer inner belt at $T_{\text{dust}} \approx 130$ K and a colder outer belt at $T_{\text{dust}} \approx 50$ K (Morales et al. 2011; Panić et al. 2013). Choquet et al. (2015) recently detected HD 377 in reprocessed archival Hubble Space Telescope (HST) scattered light images. The disk was resolved at $870 \mu\text{m}$ with the SMA, revealing a symmetric belt of emission centered at ~ 47 AU with a width of ~ 32 AU (Steele et al. 2016). Greaves et al. (2012) did not detect the disk at $7.5 - 11.5$ mm with the Green Bank Telescope (GBT), but the noise level of $14 \mu\text{Jy/beam}$ gave a 2σ upper limit on the disk flux of $< 28 \mu\text{Jy}$. No gas has been detected in the system (Geers et al. 2012). Searches with VLT/NACO have not revealed the presence of any gas giant planets with masses between 3 and $7 M_{\text{Jup}}$ and separations of $20 - 50$ AU (Apai et al. 2008).

2.2. 49 Ceti

49 Ceti is an A1V star at a distance of 59 ± 1 pc (van Leeuwen 2007) and a member of the Argus Association, indicating an age of ~ 40 Myr (Torres et al. 2008). The dust disk was resolved at $70 \mu\text{m}$ with *Herschel*/PACS (Roberge et al. 2013). SED modeling indicates that this disk has two distinct components, a cold ($T_{\text{dust}} = 62 \pm 1$ K) outer disk extending from 40 to 200 AU and a warmer ($T_{\text{dust}} = 175 \pm 3$ K) inner belt within 40 AU (Wahhaj et al. 2007; Hughes et al. 2008; Roberge et al. 2013). New ALMA observations at $850 \mu\text{m}$ are consistent with this picture and are best-fit by an inner belt of small dust grains between $\sim 4 - 60$ AU and an outer belt of larger grains between $\sim 60 - 300$ AU (Hughes et al. in prep).

In addition to the dust disk, 49 Ceti is notable for exhibiting substantial CO emission (Zuckerman et al. 1995; Dent et al. 2005; Hughes et al. 2008). Resolved (SMA) observations of CO emission in the 49 Ceti system reveal that the inner disk is devoid of gas, while the outer belt contains $0.02 \pm 0.01 M_{\oplus}$ of gas (Hughes et al. 2008). *Herschel* spectroscopy indicates that this gas cannot be primordial, and may instead be secondary material coming from the destruction of comet-like ices (Roberge et al. 2013).

2.3. HD 15115

HD 15115 (“the blue needle”) is an F2V star at 45 ± 1 pc (van Leeuwen 2007) whose space motions suggest membership in the 21 ± 4 Myr-old (Binks & Jeffries 2014) β Pictoris moving group (Moór et al. 2011). An infrared excess suggesting orbiting dust was noted in IRAS observations (Silverstone 2000). Subsequent scattered light imaging from the HST and other telescopes have resolved an asymmetric, edge-on circumstellar disk (Kalas et al. 2007; Debes et al. 2008; Rodigas et al. 2012; Mazoyer et al. 2014; Schneider et al. 2014). Observations of $850 \mu\text{m}$ emission using the James Clerk Maxwell Telescope/SCUBA-2 suggested the presence of a reservoir of large dust grains in the disk, with low temperature ($T_{\text{dust}} = 56 \pm 9$ K). Observations at 1.3 mm with the SMA resolve a belt of emission at ~ 110 AU with a width of ~ 43 AU (MacGregor et al. 2015a). In addition, the millimeter emission shows a $\sim 3\sigma$ feature aligned with the asymmetric western extension of the scattered light disk. If real, this additional feature indicates that the distribution of larger grains in the disk may be asymmetric as well.

2.4. HD 61005

HD 61005 (“the moth”) is a G8V star at a distance of 35 ± 1 pc (van Leeuwen 2007). An argument has been made for membership in the Argus Association, suggesting an age of ~ 40 Myr (Desidera et al. 2011). The presence of dust was originally inferred from a significant Spitzer infrared excess (Carpenter et al. 2005), and follow-up HST images revealed a remarkable swept-back disk in scattered light that extends from $\lesssim 10$ to 240 AU (Hines et al. 2007; Maness et al. 2009). The SED is best fit by a belt with $T_{\text{dust}} \approx 80$ K at ~ 90 AU. The disk was resolved at 1.3 mm with the SMA, and the continuum emission is fit by a narrow belt ($\Delta R/R = 0.05$) at ~ 70 AU (Ricarte et al. 2013; Steele et al. 2016). There is no indication that the dramatic scattered light asymmetry persists at millimeter wavelengths. Given the wavelength-dependent nature of the belt morphology, it is possible that the observed swept-back features result from interactions with the interstellar medium, which would be expected to affect only smaller grains (Maness et al. 2009).

2.5. HD 104860

HD 104860 is an F8 zero age main sequence star (~ 140 Myr) at a distance of 48 ± 2 pc (van Leeuwen 2007). The SED is well fit by a single temperature component at a radius of 105 AU and $T_{\text{dust}} = 33 \pm 3$ K (Najita & Williams 2005; Roccatagliata et al. 2009; Pawellek et al.

2014). The disk was resolved at 70, 100, and 160 μm with *Herschel* (Morales et al. 2013), and these observations are best fit by including a second warm, less massive dust belt at ~ 5 AU with $T_{\text{dust}} \approx 190$ K. SMA observations at 1.3 mm reveal an axisymmetric, broad belt at ~ 110 AU with a width of ~ 100 AU (Steele et al. 2016). GBT observations at 7.5–11.5 mm (Greaves et al. 2012) placed a 2σ upper limit on the disk flux of $< 24 \mu\text{Jy}$. No gas has been detected in the system (Najita & Williams 2005).

2.6. HD 141569

The HD 141569 system consists of HD 141569A, a young ~ 5 Myr-old B9.5V star at 116 ± 8 pc (van Leeuwen 2007), and a pair of low mass comoving companions with spectral types M2 and M4 located $\sim 7''.5$ away (Weinberger et al. 2000). Despite its young age, the star is surrounded by a highly evolved late-stage transition or early debris disk. The morphology of this disk is complex. Scattered light and near-infrared imaging reveal asymmetric spiral structures between ~ 175 – 210 AU and ~ 300 – 400 AU (Weinberger et al. 2000; Mouillet et al. 2001; Clampin et al. 2003; Biller et al. 2015). While this outer spiral structure is truncated at 175 AU, there is an additional inner debris belt between 10 and 50 AU (White et al. in prep.) with a dust temperature of $T_{\text{dust}} \approx 80$ K determined from SED modeling (Nilsson et al. 2010).

In addition to dust, this system contains between 20 and 460 M_{\oplus} of gas (Zuckerman et al. 1995; Thi et al. 2014). Most of this gas is associated with the outer part of the disk and distributed non-uniformly in two ring-like structures at ~ 90 and 250 AU (Dent et al. 2005). However, near-infrared observations indicate that there is additional CO gas distributed between 10 and 50 AU, commensurate with the inner debris system (Brittain & Rettig 2002; Goto et al. 2006). Recent SMA and CARMA observations at 870 μm and 2.8 mm, respectively, resolve the gas disk (Flaherty et al., submitted) and reveal a large inner hole in the CO gas distribution interior to ~ 29 AU and an outer edge at ~ 224 AU, interior to the previously imaged scattered light rings. Additionally, these observations yield $T_{\text{gas}} \sim 27$ K, lower than the dust temperature.

2.7. AU Mic

AU Mic is a nearby (9.91 ± 0.10 pc; van Leeuwen 2007) M1V star in the β Pictoris moving group, suggesting an age of 21 ± 4 Myr (Binks & Jeffries 2014). The star is surrounded by a nearly edge-on circumstellar disk extending to a radius of at least 210 AU, discovered in

coronagraphic images of scattered starlight (Kalas et al. 2004). ALMA Cycle 0 observations at 1.3 mm revealed (1) an outer belt with an emission profile that rises with radius out to 40 AU and (2) a newly recognized central peak that remained unresolved (MacGregor et al. 2013). The outer dust belt shows no evidence of asymmetries and is characterized by a dust temperature of $T_{\text{dust}} \approx 25$ K. The central peak is ~ 6 times brighter than the expected stellar photosphere, indicating an additional emission process in the inner region of the system, either a warm ($T_{\text{dust}} \approx 75$ K) planetesimal belt or a hot stellar chromosphere or corona (Cranmer et al. 2013; Schüppler et al. 2015). AU Mic is also well known to be a rich source of stellar flaring activity, notably at X-ray (Mitra-Kraev et al. 2005; Schneider & Schmitt 2010) and ultraviolet (Robinson et al. 2001) wavelengths.

3. VLA Observations

VLA observations for six of the seven sources in the sample were carried out between June and August 2014 at a wavelength of 9 mm (Ka band). Two 120-minute scheduling blocks (SBs) were observed in the D configuration (baseline lengths 0.04 to 1.03 km) for all disks except HD 141569, where only one SB was executed. HD 61005 was observed in the DnC configuration (with north-south baselines to 2.11 km, for its southern declination). We observed AU Mic, the seventh source, in June and July 2013 with two 105-minute SBs in the D configuration and one 105-minute SB in the C configuration (baseline lengths 0.05 to 3.38 km). Table 2 summarizes the essentials of these observations, including the observation dates, array configurations, number of antennas, baseline lengths, weather conditions, on-source time, and the gain calibrators used. Overall, the weather conditions were very good for these summer observations (rms of $< 6^\circ$ measured with the Atmospheric Phase Interferometer at 11.7 GHz). The total bandwidth available for all observations was 8 GHz, split into 4×2 GHz basebands centered at 30, 32, 34, and 36 GHz. The characteristic rms for these observations was $\sim 5 \mu\text{Jy}/\text{beam}$ and the typical natural weight beam FWHM was $\sim 3''$.

The data from each track were calibrated separately using the CASA software package. The passband shape was calibrated using available bright sources, mainly J0319+4130, J0609-1542, J1256-0547, and J1924-2914. Observations of 3C48 and 3C286 during each track were used to derive the absolute flux scale, with an estimated accuracy of $< 10\%$. Imaging and deconvolution were performed with the `clean` task in CASA (version 4.3.1).

4. Results of the VLA Observations

Figure 1 shows the VLA 9 mm images for the six detected debris disks in the sample. HD 377 was undetected. For the detected disks, the peak signal-to-noise ratio achieved ranges between $\sim 4\sigma$ (HD 15115 and HD 104860) and $\sim 16\sigma$ (HD 141569).

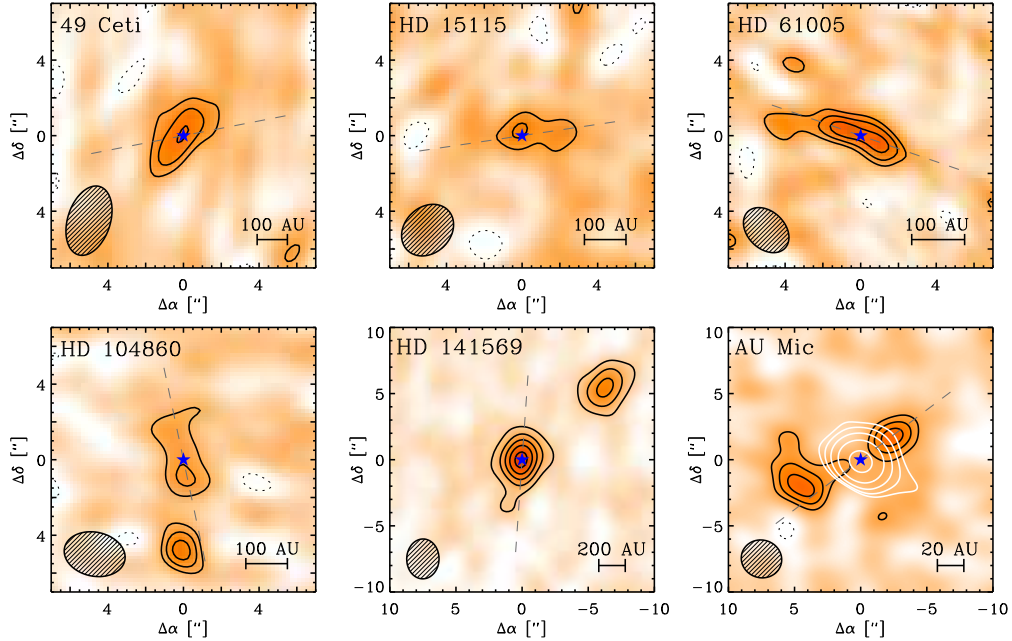


Fig. 1.— Images of the 9 mm continuum emission from the six debris disks detected in the VLA sample. Contour levels are in steps of $[2, 3, 4, 6] \times \text{rms}$ for all images, except HD 141569 (lower center) where contours are in steps of $3 \times \text{rms}$ (characteristic rms $\sim 5 \mu\text{Jy}$). The white contours in the AU Mic image (lower right) mark the subtracted stellar component in steps of $[10, 20, 40, 80, 160] \times \text{rms}$. The ellipse in each lower left corner indicates the synthesized beam size. The star symbol marks the position of the stellar photosphere. The dashed gray line indicates the position angle of the disk determined from previous optical, near-infrared, or millimeter imaging and listed in Table 1.

The 49 Ceti and HD 141569 disks are unresolved by these observations. The HD 15115, HD 61005, and HD 104860 disks are all marginally resolved, appearing extended in the direction of their position angles as determined from previous optical, near-infrared, and millimeter imaging. Indeed, the HD 15115 disk shows a hint (at a $\sim 2\sigma$ level) of the same asymmetric western extension seen in previous optical and millimeter imaging (MacGregor et al. 2015a). For all five of these disks, the total flux density was determined by integrating the surface brightness over the area showing continuum emission at $\gtrsim 2\sigma$ above the background rms in the image. The total uncertainty on the 9 mm flux density was taken to be the rms noise

measured for the image added in quadrature with the 10% uncertainty in the absolute flux calibration. For HD 377, we obtain a 3σ upper limit on the total disk flux density. Table 3 lists the synthesized beam size and position angle, the measured 9 mm flux density, and the rms for all of the sources in the sample.

AU Mic is the only disk that is well resolved in the sample. The C configuration affords high angular resolution (beam size $< 1''$, corresponding to < 10 AU at the distance of AU Mic) relative to the extent of the disk. This high resolution allows us to separate emission from the the central star and the disk. The star is very active at radio wavelengths, flaring on timescales shorter than the scheduling blocks. We were able to isolate the disk emission by subtracting a time-dependent point source model from the data to account for the stellar emission. In doing this, we could not avoid subtracting out some disk emission co-located with the star. We estimated the total flux density as for the other disks in the sample. However, the result obtained should be considered a lower limit to the disk emission. A detailed account of the stellar emission observed in the AU Mic system is included in the appendix.

5. Determining the Slope of the Grain Size Distribution q

We adopt the method of Ricci et al. (2012, 2015b) who used ATCA observations at 7 mm to constrain the millimeter grain size distribution of six debris disks. Since the thermal dust emission from debris disks is optically thin, the flux density is given by $F_\nu \propto B_\nu(T_{\text{dust}})\kappa_\nu M_{\text{dust}}/d^2$, where $B_\nu(T_{\text{dust}})$ is the Planck function at the dust temperature T_{dust} , $\kappa_\nu \propto \nu^\beta$ is the dust opacity, expressed as a power law at long wavelengths, M_{dust} is the total dust mass in the disk, and d is the distance. Draine (2006) derived a relation between β , the dust opacity power law index, and q , the grain size distribution parameter: $\beta = (q - 3)\beta_s$, where, β_s is the dust opacity spectral index of small (i.e. much smaller than the observing wavelength) particles. For size distributions that follow a power law with $3 < q < 4$ from blow-out grain sizes (on the order of $\sim \mu\text{m}$) to larger planetesimals ($\sim 1 - 100$ km), $\beta_s = 1.8 \pm 0.2$, consistent with observations of both diffuse and dense interstellar clouds. It should be noted, that given the restrictive assumption of $3 < q < 4$, this relation could prove inaccurate for any disks that have a size distribution index outside of this range. Additionally, for dust compositions with large fractions of amorphous carbons or ices, values of β_s can drop to ~ 1.4 (e.g. ‘cel800’ produced by the pyrolysis of cellulose at 800°C in Draine 2006), resulting in higher q values for a given β . For a representative case, where $\beta = 0.5$, $q = 3.28$ and 3.36 for $\beta_s = 1.8$ and 1.4 , respectively. The change in q due to a change in β_s is ~ 0.08 in this case, comparable to the uncertainties on q derived by

our analysis. Since we do not expect this effect to be large, and given our limited knowledge of the grain compositions in the debris disks in our sample, we assume $\beta_s = 1.8$ for the purposes of our analysis. This relation between β and q has been found to be very accurate for different dust models considered in the literature to interpret the millimeter wavelength emission of young circumstellar disks (see e.g. D’Alessio et al. 2001; Ricci et al. 2010b,a).

For debris disks around solar-type and earlier stars, the dust is typically warm enough ($k_B T_{\text{dust}} \gg h\nu$) for the Planck function at long wavelengths to reduce to the Rayleigh-Jeans approximation $B_\nu(T_{\text{dust}}) \propto \nu^2$. A more accurate expression can be obtained by approximating the Planck function as a power law $B_\nu(T_{\text{dust}}) \propto \nu^{\alpha_{\text{Pl}}}$, where $\alpha_{\text{Pl}} = \alpha_{\text{Pl}}(T_{\text{dust}}) \lesssim 2$ (and $= 2$ in the Rayleigh-Jeans limit). Given two frequencies, the spectral index α_{Pl} of the Planck function between ν_1 and ν_2 can be expressed as

$$\alpha_{\text{Pl}} = \left| \frac{\log(B_{\nu_1}/B_{\nu_2})}{\log(\nu_1/\nu_2)} \right| \quad (1)$$

Substituting the Taylor expansion of B_ν to second order yields the following approximation for the spectral index:

$$\alpha_{\text{Pl}} \approx 2 + \frac{\log\left(\frac{2k_B T_{\text{dust}} - h\nu_1}{2k_B T_{\text{dust}} - h\nu_2}\right)}{\log(\nu_1/\nu_2)} \quad (2)$$

For our purposes, the spectral index of the Planck function can be approximated by the Rayleigh-Jeans solution with a correction that depends on the dust temperature T_{dust} and observing frequencies used to determine the millimeter spectral index.

Observationally, the flux density of debris disks at millimeter and centimeter wavelengths can be described by a simple power law $F_\nu \propto \nu^{\alpha_{\text{mm}}}$, where $\alpha_{\text{mm}} = |\log(F_{\nu_1}/F_{\nu_2})/\log(\nu_1/\nu_2)|$.

Combining these relationships provides a simple expression for the slope of the grain size distribution, q as a function of α_{mm} , α_{Pl} , and β_s :

$$q = \frac{\alpha_{\text{mm}} - \alpha_{\text{Pl}}}{\beta_s} + 3 \quad (3)$$

Thus, by measuring the millimeter spectral index, α_{mm} , and by inferring α_{Pl} from the dust temperature for each disk, we can determine the slope of the grain size distribution, q .

5.1. Estimated q Values for the Complete Sample

We complement the VLA 9 mm observations of the seven debris disks with ATCA 7 mm observations of eight additional debris disks (system characteristics listed in Table 1) analyzed in previous papers. Results for Fomalhaut were presented by Ricci et al. (2012), and results for α^1 Eri, β Pic, HD 95086, HD 107146, and HD 181327 were presented by Ricci et al. (2015b). For HD 181327 and HD 95086, we have recalculated spectral indices given newly available ALMA measurements. For α^1 Eri, we have recalculated the spectral index using the flux measurement at 870 μ m from APEX (Liseau et al. 2008), to be closer to the Rayleigh-Jeans regime for a more accurate determination of the spectral slope. Su et al. (2015) suggest that previous flux measurements of HD 95086 are likely contaminated by emission from the extragalactic background. Any such background galaxies are included within the ATCA beam and not resolved from the disk. Given this situation, which may well apply to other sources, we simply use the total flux density within the beam in the analysis. The ϵ Eridani debris disk, which was not detected at 7 mm with ATCA (MacGregor et al. 2015b), provides an upper limit on the spectral index in combination with resolved observations at 1.3 mm from the SMA. We have also included archival ATCA observations of AK Sco, a ~ 18 Myr-old binary system with a massive ($\sim 5 - 10 M_{\text{Jup}}$) circumbinary disk of gas and dust (Czekala et al. 2015). Given its age, there is some debate as to whether this system is a long-lived disk of primordial origin or a second-generation debris disk. We choose to include it in the sample to examine the effects gas might have on collisional cascade properties (see Section 5.2). We used the `uvfit` routine in Miriad to fit a point source model to the ATCA 7 mm AK Sco visibilities and obtained a total flux density of $F_{7\text{mm}} = 430.0 \pm 18.2 \mu\text{Jy}$. Figure 2 shows images of the 7 mm continuum emission from the debris disks detected by ATCA (excluding Fomalhaut).

Table 4 lists a previously reported flux density of each disk in the sample at a given (sub)millimeter wavelength, and we use these values combined with the VLA 9 mm and ATCA 7 mm fluxes to determine a millimeter spectral index, α_{mm} . Eight of the disks in the sample have flux measurements from ALMA data available. For the remaining seven disks, we used flux measurements from the SMA, JCMT/SCUBA, and APEX as available. The reported uncertainties for these (sub)millimeter flux measurements include a 10% uncertainty in the absolute flux density calibration added in quadrature to the statistical uncertainties. Table 4 also presents the dust temperature (T_{dust}), the spectral index of the Planck function (α_{Pl}), and the slope of the grain size distribution (q) derived using Equation 3. For all of the disks, the dust temperature was inferred by assuming radiative equilibrium with the central star: $T_{\text{dust}} = (L_*/16\pi\sigma R_{\text{dust}}^2)^{1/4}$. Here, we used established stellar properties to determine L_* and resolved (sub)millimeter imaging to estimate a characteristic radius for the dust, R_{dust} . The uncertainties on R_{dust} and T_{dust} are conservatively estimated to be 20% and 10%,

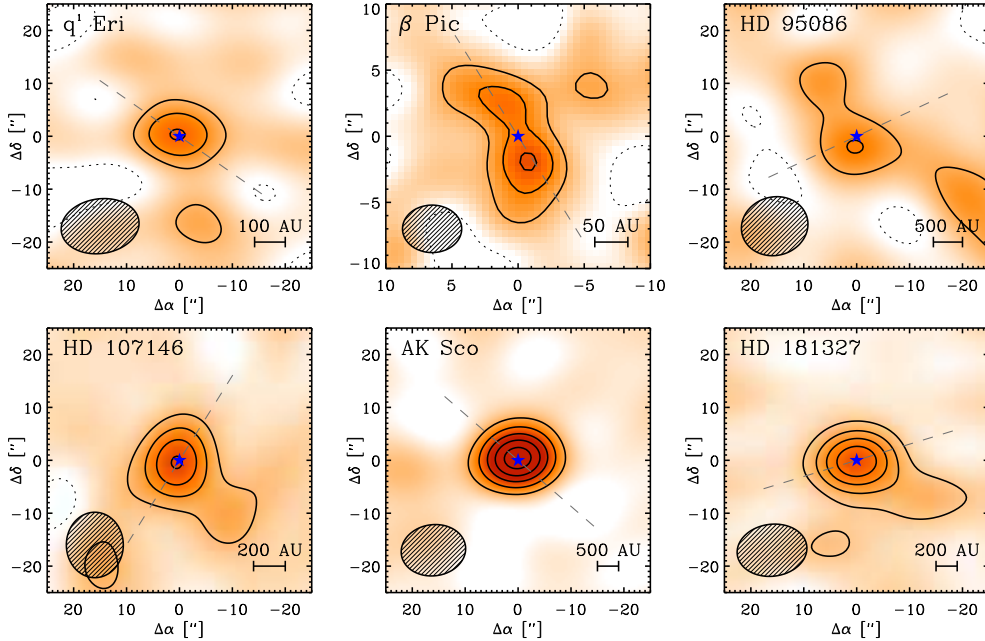


Fig. 2.— Images of the 7 mm continuum emission from six debris disks detected in the ATCA sample. Contour levels are in steps of $2 \times \text{rms}$ for all images, except AK Sco (lower center) where contours are in steps of $4 \times \text{rms}$ (characteristic rms $\sim 14 \mu\text{Jy}$). The ellipse in each lower left corner indicates the synthesized beam size. The star symbol marks the position of the stellar photosphere. The dashed gray line indicates the position angle of the disk determined from previous optical, near-infrared, or millimeter imaging and listed in Table 1.

respectively. Given T_{dust} and the two frequencies used to measure α_{mm} , we determined α_{pl} for each disk using the relationship derived in Equation 2. The final uncertainty on q results from propagating the errors on α_{mm} , α_{pl} , and β_S .

For the complete sample, q values range from 2.84 (HD 141569) to 3.64 (HD 104860). The weighted mean of these q values is $\langle q \rangle = 3.36 \pm 0.02$. This result is consistent with previous work by Ricci et al. (2015), which presented results for five of the debris disks included in this larger sample and obtained a weighted mean of $\langle q \rangle = 3.42 \pm 0.03$.

5.2. Trends in q with Stellar and Disk Properties

With this larger sample, we can not only determine a weighted mean value of q , but begin to look for trends with stellar and system characteristics. The stars in the sample span a wide range of ages (5–4800 Myr) and spectral types (A–M). Table 1 lists the characteristics

of the stars in the full sample, including age, spectral type, luminosity, distance, and whether or not gas has been detected in the disk.

We first consider trends with stellar properties, namely age and spectral type. There does not seem to be any correlation between system age and grain size distribution. For disks with estimated ages < 100 Myr (49 Ceti, HD 15115, HD 61005, HD 141569, AU Mic, β Pic, HD 95086, Ak Sco, and HD 181327), the weighted mean is $\langle q \rangle = 3.36 \pm 0.02$. Disks with estimated ages > 100 Myr (HD 377, HD 104860, η Eri, ϵ Eri, HD 107146, and Fomalhaut) have a weighted mean of $\langle q \rangle = 3.35 \pm 0.02$, consistent with the other subsample within the uncertainties. A Kolmogorov-Smirnov (K-S) test gives a 85% probability that these two subsamples are drawn from the same distribution. However, we notice a tentative trend with spectral type. If we arbitrarily choose to separate the sample into two groups by spectral type, then the weighted mean is $\langle q \rangle = 3.40 \pm 0.02$ for stars with spectral types A–F (49 Ceti, HD 15115, HD 61005, HD 104860, HD 141569, η Eri, β Pic, HD 95086, AK Sco, and HD 181327) and $\langle q \rangle = 3.30 \pm 0.03$ for spectral types G–M (HD 377, HD 61005, AU Mic, ϵ Eridani, and HD 107146). Given the uncertainties, these two subsamples differ in q by $\sim 3\sigma$. The clear outlier in the sample is HD 141569, with a q value of 2.84 ± 0.03 (discussed in Section 6.4). If we exclude this source from the sample, the weighted mean for A–F stars is $\langle q \rangle = 3.45 \pm 0.02$, different from the other subsample by $\sim 5\sigma$. A Spearman’s rank correlation measure of statistical dependence between two variables indicates that this trend is significant at 96% confidence. A K-S test gives a probability of only 15% that these two subsamples are drawn from the same distribution. Given the small number statistics (there are noticeably fewer late type stars in the sample), we cannot draw any firm conclusions. However, this is suggestive that stars with later spectral types may exhibit shallower grain size distributions. Interestingly, Pawellek et al. (2014) also note a trend of increasing q values for more luminous stars, determined from mid- to far-infrared observations probing smaller grain sizes.

It is also plausible that characteristics of the disks themselves, regardless of stellar properties, might affect the grain size distribution. Four of the disks in the sample have robust detections of gas: 49 Ceti, HD 141569, β Pic, and AK Sco. For these disks with gas, $\langle q \rangle = 3.33 \pm 0.03$ including HD 141569, and $\langle q \rangle = 3.42 \pm 0.03$ omitting HD 141569, neither value differing from the mean of the full sample by $> 3\sigma$. The K-S probability for these two subsamples is 92%. However, since there are only four disks with detections of gas in the sample, observations of more debris disks are needed to address the effect of disk gas on grain size distribution.

6. Discussion

We have performed interferometric observations of a sample of seven debris disks at 9 mm with the VLA and supplemented them with observations of eight debris disks observed with ATCA at 7 mm. By combining these long wavelength flux densities with previous (sub)millimeter measurements, we have determined a millimeter spectral index and inferred the slope of the grain size distribution, q . The weighted mean of the q values in the complete sample is $\langle q \rangle = 3.36 \pm 0.02$.

We now compare these new results for the full sample to theoretical models of collisional cascades. In particular, we consider the effects of incorporating alternative velocity distributions (Section 6.1), material strengths (Section 6.2), and radiation pressure blowout (Section 6.3) on the resulting grain size distributions in debris disks.

6.1. Comparison to Collisional Models

The reference model for dust production in debris disks is the steady state catastrophic collisional cascade. In this model, smaller ‘bullets’ shatter larger ‘targets’ through collisions. Assuming conservation of mass, this shattering recipe leads to a power law size distribution of colliding bodies with radius a within the disk, $n(a) \propto a^{-q}$. A detailed description of the analytic treatment of collisional cascades can be found in Pan & Sari (2005) and Pan & Schlichting (2012).

The benchmark model of collisional cascades is presented by Dohnanyi (1969). Using laboratory experiments, Dohnanyi formulated a model of collisions in the Asteroid Belt, where bodies dominated by material strength have an isotropic velocity dispersion and collisions occur between bodies of roughly the same size. Given these assumptions, Dohnanyi obtains the classic result of $q = 7/2$ in steady-state.

If the assumption that the bodies participating in the collisional cascade have a single velocity dispersion regardless of size is relaxed, then steeper grain size distributions can be produced. Pan & Schlichting (2012) extend the Dohnanyi (1969) formulation of collisional cascades by accounting for viscous stirring, dynamical friction, and collisional damping in addition to the mass conservation requirement already discussed. For collisions between equal-sized, strength-dominated bodies, accounting for a size-dependent velocity distribution where velocity decreases with decreasing particle size yields $3.64 \leq q \leq 4$. If, instead, the velocity *increases* with decreasing particle size, then shallower size distributions are produced. This scenario makes sense for particles close to the blowout size, where radiation pressure strongly affects the particles’ velocities. Given a population of grains with velocity

function $v \propto a^p$ and material strength parameterized by $Q_D^* \propto a^\gamma$, Pan & Schlichting (2012) give a simple formulation for q as a function of γ and p : $q = \frac{21+\gamma-2p}{6+\gamma-2p}$. For small grains ($a \lesssim 1$ mm) strongly affected by radiation pressure, the collision velocities are expected to be proportional to the radiation-pressure induced eccentricities and $p \approx -1$. For strength-dominated particles, $0 \geq \gamma > -1/2$. Given a representative value of $\gamma = -0.3$, this formulation yields $q = 2.95$. For the somewhat larger (sub)millimeter particles probed by our observations, it is plausible to expect q values somewhere between this estimation and Dohnanyi’s $q = 3.5$.

Gáspár et al. (2012) explored the evolution of collisional cascades in debris disks using numerical models. They varied a total of 21 variables in their models describing the geometry of the system, the strength of the colliding bodies, and the outcome of collisions. In steady-state, these calculations yield a range of $q \approx 3.64 - 4.33$.

A number of other numerical models incorporate more realistic physics in order to model the grain size distributions for specific systems. Löhne et al. (2012) use the ACE (Analysis of Collisional Evolution, see e.g. Krivov et al. 2013) code, which takes into account grain material strength, mutual gravity, and the relative orientation of the orbits of colliding particles, to model the size distribution for HD 207129. Schüppler et al. (2014) and Schüppler et al. (2015) use the same numerical code to model the size distributions of HIP 17439 and AU Mic, respectively. For grain sizes between $10 \mu\text{m}$ and 1 mm, these models yield q values between 3.3 and 3.4 for all three systems. Additionally, Thébault & Wu (2008) suggest that the grain size distribution should depend on the degree of dynamical excitation of the dust-producing planetesimals. In disks with parent bodies in low-eccentricity, low-inclination orbits, the resulting size distribution should be flatter than classical collisional cascade models. Pawellek & Krivov (2015) use the ACE code to examine this prediction and obtain $q \sim 3$ for grains of size $a = \frac{a_{\text{bl}}}{2e}$, where a_{bl} is the blowout size and e is the mean eccentricity of parent bodies. For larger grains, $100 < a < 1000 \mu\text{m}$, the slope is closer to $\sim 3.3 - 3.4$.

Figure 3 shows the distribution of q values from the fifteen debris disks in the sample along with the steady-state model predictions of Dohnanyi (1969), Pan & Sari (2005), Schüppler et al. (2015), Gáspár et al. (2012), and Pan & Schlichting (2012). The weighted mean of the sample, $\langle q \rangle = 3.36 \pm 0.02$, is comparable to the classic Dohnanyi (1969) solution of $q = 3.5$, but still differs formally by $\sim 7\sigma$. Models of specific debris disk systems using the ACE numerical code (e.g. Löhne et al. 2012; Schüppler et al. 2014, 2015) yield q values between $\sim 3.3 - 3.4$, lower than classical collisional cascade models and comparable to the weighted mean of our sample. Gáspár et al. (2012) obtain some q values from their models that are comparable to the observed mean value, but only by increasing the scaling of the strength regime, S , to $\gg 10^8$ erg/g, in excess of the fiducial value of 3.5×10^7 erg/g

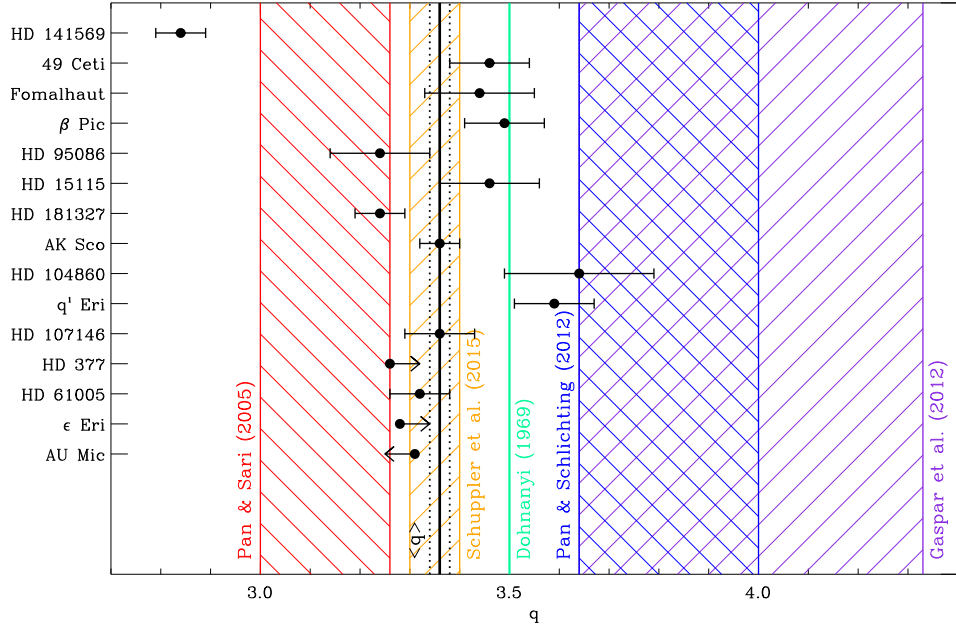


Fig. 3.— Distribution of power law index q values for the full sample of debris disks together with model predictions. Black data points indicate the values for the individual disks in the sample, with the weighted mean and uncertainty, $q = 3.36 \pm 0.02$, shown by the solid and dotted black lines, respectively. Stars have been ordered by luminosity from top to bottom (see Table 1 for specific luminosity values). The solid lines and dashed regions indicate different model predictions: (red) ‘rubble pile’ planetesimals not dominated by material strength (Pan & Sari 2005), (orange) results of the ACE numerical model for AU Mic (Schüppler et al. 2015), (green) the classic Dohnanyi (1969) result, (purple) numerical results of Gáspár et al. (2012), and (blue) incorporating a size-dependent velocity distribution (Pan & Schlichting 2012).

(Benz & Asphaug 1999). All of the models from Pan & Schlichting (2012) that incorporate a size-dependent velocity distribution where velocity decreases with decreasing particle size yield q values greatly in excess of the observed q values for all of the individual disks in our sample. However, the velocities in the grain size range of interest could instead increase with decreasing particle size due to radiation pressure. As is shown above, such a velocity distribution could reproduce q values comparable to our results.

We can also explore the effect of additional parameters on the grain size distribution, namely the strength of the colliding bodies and deviations from a strict power law introduced by a small-size cutoff due to radiation pressure. This is done in the following two sections.

6.2. Varying the Strength of Colliding Bodies

Models of collisions between rubble pile grains can predict q values comparable to our results. However, it is unclear if these parameters are realistic for the colliding grains probed by our millimeter observations of debris disks. The idea of collisions between strengthless rubble piles was proposed to explain observations of comets and Kuiper Belt Objects (KBOs), which are on the order of several kilometers in size (Asphaug & Benz 1996; Jewitt & Sheppard 2002). Our observations probe millimeter to centimeter sized grains, which are typically assumed to be rocky and strength dominated. Analytical and numerical calculations indicate that bodies do not become gravity-dominated until they are larger than ~ 1 km (Wyatt et al. 2011). Furthermore, laboratory experiments show that the strength of small rocky particles does not vary significantly with particle size, scaling as $a^{-0.4}$ (Housen & Holsapple 1999). However, one could imagine that millimeter and centimeter sized grains might be more similar to loose conglomerates than rocky pebbles, and thus might exhibit strength scaling laws more similar to large rubble piles. In fact, measurements of the optical polarization of the AU Mic debris disk taken with *HST/ACS* suggest that the grains in the disk are highly porous (91 – 94%), more like ‘bird nests’ (Graham et al. 2007).

To produce the models discussed in Section 6.1, we require that the bodies participating in the collisional cascade are strength-dominated. If the colliding bodies are more like ‘rubble piles,’ held together by gravity instead of material strength, we can replace the destruction criterion that collisions occur between bodies of the same size with the requirement that the kinetic energy of the bullet be equal to the gravitational energy of the target. Pan & Sari (2005) derive a range of q values $3.0 \leq q \leq 3.26$ for such a collisional population, lower than the steady-state collisional cascade predictions of Dohnanyi (1969).

6.3. Wavy Distributions Produced by a Small-Size Cutoff

Grains within a debris disk are continually subject to radiation pressure from the central star. Large grains are less affected by this radiation pressure and remain in bound orbits, while smaller grains are placed in hyperbolic orbits. A ‘blowout’ size, a_{bl} , can be defined as the grain size for which the force due to radiation pressure (F_{rad}) is half the force from gravity (F_{g}) and $F_{\text{rad}}/F_{\text{g}} \gtrsim 0.5$. For grains smaller than this blowout size, bound orbits are impossible and grains are removed from the disk.

Dohnanyi (1969) did not include a small-size cutoff in his theoretical framework to account for the removal of grains smaller than the blowout size. Including such a cutoff superimposes waves or ripples on the predicted power law distribution. The lack of grains

smaller than a_{bl} , causes the equilibrium number of blowout-sized grains to be enhanced. In turn, this results in an enhanced destruction rate of grains with sizes typically destroyed by blowout-sized grains. Consequentially, the absence of these grains produces a higher equilibrium number of grains that would have been destroyed by them. This ripple effect propagates upwards through the grain size distribution. Previous numerical simulations have produced and discussed this wavy pattern (Campo Bagatin et al. 1994; Thébault et al. 2003; Krivov et al. 2006; Wyatt et al. 2011). The wavelength and amplitude of these waves depends strongly on the collisional velocities and properties of the colliding bodies.

A realistic debris disk, however, is not expected to have a sharp cutoff at small grain sizes. Krivov et al. (2006) note that dispersion in densities and fragmentation energies within an inhomogeneous grain population will likely weaken or smear any waves produced in the size distribution. Additionally, including erosive or cratering collisions has a clear impact on the grain size distributions (Thébault & Augereau 2007; Kenyon & Bromley 2016), washing out ripples at grain sizes much above the blowout size.

Within the analysis of this paper, we have assumed that the size distribution of particles within a debris disk is a power law, $n(a) \propto a^{-q}$. Given the wavy size distributions predicted by some numerical models, however, it is plausible that the power law size distribution we measure between millimeter and centimeter wavelengths does not reflect the full distribution from micron to kilometer sizes. In order to explore the effect of ripples on the measured grain size distribution further, we have replicated with small modifications the numerical model presented by Wyatt et al. (2011) and implemented analytically by Kenyon & Bromley (2016). The details of the model are described in Section 6.3.1 and the results and implications are presented in Section 6.3.2. This simple model provides a useful illustration of how possible modulations in the grain size distribution would be reflected in the observed opacity spectrum. However, the results should not be over interpreted, given the range of effects that may damp such modulations in more realistic systems.

6.3.1. A Steady State Model with a Small-Size Cutoff

We define a population of planetesimals divided into N bins spaced logarithmically in size, where the mass and size of the k th bin are m_k and a_k , respectively. The largest bin is defined to be $k = 1$ and size decreases with increasing k such that $a_{k+1}/a_k = 1 - \delta$, with $\delta = 0.01$. The size of the smallest bin is defined as the blowout size, a_{bl} , and the size of the largest bin is fixed at 10^4 m. Like Wyatt et al. (2011), we assume a steady state where the mass loss rate per logarithmic bin is constant and the mass in each bin is defined as $m_k = C/R_k^c$, where C is some arbitrary constant and R_k^c is the collision rate in bin k . The

discrete form of the collision rate can be expressed as

$$R_k^c = \sum_{i=1}^{i_{ck}} \frac{3m_i}{2\rho\pi a_i^3} (a_k + a_i)^2 P_{ik}, \quad (4)$$

where ρ is the particle density, P_{ik} is the intrinsic collision probability between particle i and k defined as $\pi v_{\text{rel}}/V$, v_{rel} is the relative collision velocity, and V is the total volume through which the planetesimals are moving. The smallest impactors that can catastrophically destroy particles of size a_k have size $X_c a_k$, where $X_c = (2Q_D^*/v_{\text{rel}}^2)^{1/3}$ and Q_D^* is the collision energy required to eject half the mass from a pair of colliding bodies.

Using this formalism, the mass in each bin can be solved for analytically, beginning with the smallest bin, $k = N$. Since there are no smaller impactors available, only bodies of size a_N are involved in the collisional cascade. Thus, R_N^c can be solved for simply:

$$R_N^c = \left(\frac{6P_{NN}}{\rho\pi a_N} \right) \times m_N = A_N m_N \quad (5)$$

The mass in bin N is then $\sqrt{C/A_N}$. Next, we can consider bin $N - 1$. In this bin, the summation in Equation 4 has two terms:

$$R_k^c = A_{k+1} m_{k+1} + A_k m_k \quad (6)$$

Since we already determined the mass in bin N , we know the first term $A_{k+1} m_{k+1} = B_k$. We can then simplify Equation 6 to $R_k^c = B_k + m_k A_k$. The mass in bin $N - 1$ is then found by solving a quadratic equation:

$$m_k^2 A_k + m_k B_k - C = 0 \quad (7)$$

Moving up to bins of larger size, R_k^c always contains two terms, a sum over all collisions with smaller particles and $m_k A_k$ for the current bin. Thus, the mass in each bin is found simply by solving Equation 7 for every bin. In this formulation, the shape of the steady-state distribution is independent of the total mass.

Once we have determined the steady-state number of grains in each bin, we calculate grain opacities to determine whether the resulting wavy number distribution translates to an observable effect. We assume the same grain compositions as Ricci et al. (2010b) that contain 7% silicates, 21% carbon, and 42% water ice by volume, and have 30% porosity. The details

of these assumptions are not important to demonstrate the resulting effect on the opacities. For each size bin, we use the Mie scattering code implemented by Dullemond & Dominik (2004) for use in RADMC, a code for dust continuum radiative transfer. The output of this code is an opacity spectrum for each individual grain size in our model. To determine the ensemble opacity at each wavelength, we then calculate a mass-weighted average over all grain sizes given the steady-state size distribution.

The final result of this procedure is the ensemble opacity of a given population of grains as a function of wavelength. For our observations, we measure flux density at two wavelengths in order to determine the millimeter spectral index, α_{mm} . If the dust opacity is a simple power law, ν^β , we can infer $\beta = \alpha_{\text{mm}} - 2$ from our observations so long as the disk emission is optically thin and in the Rayleigh-Jeans regime. Given the final ensemble opacity spectrum from our models, we can determine the power law index, β , between any two wavelengths we might observe at. By computing β for a range of models and wavelengths corresponding to the observations presented in this study, we can examine the scatter in β (and thus q) we might expect due to waves produced by a small-size cutoff in the grain size distribution.

6.3.2. Variations in Spectral Indices Due to Waves in Grain Size Distributions

To determine the expected scatter in the observed millimeter-centimeter spectral index from waves superimposed on the power law grain size distribution, we considered three free parameters in our model: a_{bl} , v_{rel} , and Q_D^* . For debris disks, $v_{\text{rel}} \gtrsim 1 \text{ km s}^{-1}$ (Krivov 2007); we calculated models for a range of 1 to 6 km s^{-1} . We considered both constant $Q_D^* = Q_s$ and a power law dependence on grain size, $Q_D^* = Q_s r^{\beta_s}$. For rocky objects dominated by material strength, $Q_s = 6 \times 10^3 \text{ J kg}^{-1}$ and $\beta_s = -0.40$ (Benz & Asphaug 1999). The blowout size, a_{bl} is expected to vary between $\sim 1 - 10 \mu\text{m}$ for the disks in the sample.

Figure 4 shows the resulting size distribution (left panel) and ensemble opacity as a function of wavelength (right panel) for two example models with blowout size, a_{bl} , of 1 μm and 10 μm . For both models, we fixed $v_{\text{rel}} = 5 \text{ km s}^{-1}$ and $Q_D^* = 6 \times 10^3 \text{ J kg}^{-1}$. The waves produced in the size distribution by the changing blowout size are seen as muted features in the dust opacity curves. For these two models, blowout sizes of 1 and 10 μm produce dust opacity power law indices of $\beta = 0.63$ and 0.88, respectively. For lower relative velocities ($v_{\text{rel}} \sim 1 \text{ km s}^{-1}$) the waves are damped at long millimeter and centimeter wavelengths and the change in β is negligible. For the full range of free parameters we explored, the resulting values of β ranged from 0.5 to 1.1, comparable to the spread in our complete sample of debris disks, $-0.20 \lesssim \beta \lesssim 1.15$. This is not a definitive explanation for the trend we see in spectral index as a function of stellar type, but it suggests that the waves produced by introducing a

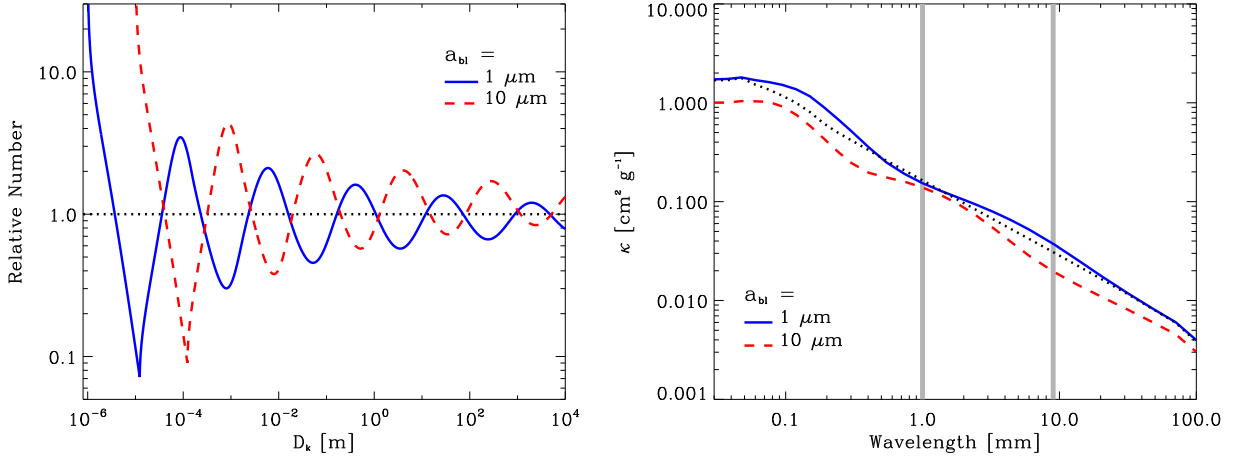


Fig. 4.— *(left)* Comparison of the relative size distribution, $n(a)/n(a)_{\text{pl}}$, for a steady-state collisional cascade with a blowout size a_{bl} of $1 \mu\text{m}$ (blue solid line) and $10 \mu\text{m}$ (red dashed line). For both models, we have divided the analytic number distribution, $n(a)$, by the expectation for a power law distribution, $n(a)_{\text{pl}} \propto a^{-3.5}$, to show the waves introduced by the small-size cutoff more clearly. The expected power law size distribution, $n(a)_{\text{pl}}$, is indicated by the dotted black line. For all models, we assume $Q_D^* = 6 \times 10^3 \text{ J kg}^{-1}$ and $v_{\text{rel}} = 5 \text{ km s}^{-1}$. *(right)* The resulting ensemble opacity as a function of wavelength for a $1 \mu\text{m}$ blowout size (blue solid line) and a $10 \mu\text{m}$ blowout size (red dashed line). Again, the dotted black line indicates the expected ensemble opacity for the power law size distribution with no waves. The gray lines indicate the wavelengths of our (sub)millimeter and VLA observations used to determine the millimeter spectral index, α_{mm} .

cutoff at small grain sizes could introduce observable scatter in the values of β , and thus q , similar to that seen in the measured spectral indices. It is also possible that grain porosity could change with particle size and create damped resonances as a function of wavelength that might produce structure in the opacity spectrum and result in low values of β . Recent work suggests that K–M (and possibly G) stars do not exhibit a blowout limit for plausible dust compositions (e.g. Reidemeister et al. 2011; Vitense et al. 2012; Schüppler et al. 2015). The lack of a sharp size cutoff for such stars could further damp any waves in the grain size distribution, possibly contributing to the inferred shallower size distribution for these late-type stars.

6.4. Stellar Emission Components

A potential source of bias is our implicit assumption that all of the emission we detect at long wavelengths comes from the dusty debris. If the measured flux densities at long

wavelengths include emission from any additional mechanisms, then we will underestimate the true millimeter spectral index and thus the size distribution power law index, q . As discussed in the appendix, the AU Mic system exhibits significant emission from stellar activity at both 1.3 and 9 mm that can be explained by models of a hot stellar corona or chromosphere. Given this stellar activity, the presence of an asteroid belt (MacGregor et al. 2013; Schüppler et al. 2015) is no longer needed to explain the previously reported compact millimeter emission. In this system, we were able to distinguish the excess stellar emission from the disk and subtract it using a time-dependent model. Only three other systems are well enough resolved by the centimeter observations to address this issue, β Pic, ϵ Eridani, and Fomalhaut. Indeed, while the ϵ Eridani debris disk is not detected at centimeter wavelengths, the central star exhibits excess emission attributable to a hot chromosphere (MacGregor et al. 2015b). The Fomalhaut system shows a central peak at 7 mm distinct from the cold, outer debris belt whose origin is unclear (Ricci et al. 2012). In the eleven unresolved systems in the sample, we cannot separate disk dust emission from any stellar contamination, if present.

The clear outlier in the sample is HD 141569, with a q value of 2.84 ± 0.03 , well below the weighted mean of our complete sample and the classic Dohnanyi prediction. In order to increase this q -value to 3.50, as predicted by Dohnanyi (1969), more than 90% of the emission measured at 9 mm would have to come from contamination from a stellar component, vastly in excess of the expected photospheric flux at these long wavelengths. However, a contribution from an active stellar chromosphere or corona cannot be ruled out. While this system has been imaged with ALMA at 870 μm , it remains unresolved (White et al. in prep), so we have no constraints on the millimeter or centimeter stellar emission. The HD 141569 disk is the youngest source in the sample with an age of ~ 5 Myr and contains a significant amount of gas. Furthermore, HD 141569 has two nearby M dwarf companions (Weinberger et al. 2000) with their own associated radio emission (see Figure 1). It is possible that one or all of these system characteristics contributes to the low q value measured, or that the central region of the disk is optically thick at these wavelengths. For example, gas drag and other transport mechanisms (Poynting-Robertson or stellar wind drag) would tend to flatten the size distribution of affected grains. Wyatt et al. (2011) show that the resulting q value is $\alpha_r - 1$, where α_r is the slope of the redistribution function or the mass distribution of fragments produced in collisions. Given $\alpha_r = 4$, the expected q value for a system with gas drag would be ~ 3 , much flatter than the classic Dohnanyi prediction of $q = 3.5$ and more comparable to the result for HD 141569.

In order to conclusively determine if the flux measurement of HD 141569 or any of the other unresolved disks in the sample are contaminated by coronal or chromospheric emission, observations at millimeter and centimeter wavelengths with higher angular resolution are

needed. A growing number of nearby solar type stars, including α Cen A and B (Liseau et al. 2015) and ϵ Eridani (MacGregor et al. 2015b), have all been seen to exhibit excess emission at long wavelengths attributable to a hot chromosphere. However, except for AU Mic, none of the other debris disks in our sample that have been resolved with ALMA show any evidence for an additional strong stellar emission component.

7. Conclusions

We present new VLA observations at 9 mm of a sample of seven debris disks. Using the best available flux measurements at (sub)millimeter wavelengths, we place tight constraints on the millimeter/centimeter spectral indices. We combine these with archival ATCA observations at 7 mm of an additional eight debris disks building on the work of Ricci et al. (2015a) and Ricci et al. (2012) to infer the dust grain size distribution power law index, q .

1. For the full sample, the weighted mean for the slope of the power law grain distribution is $\langle q \rangle = 3.36 \pm 0.02$, with a range of 2.84 to 3.64. This result is closest to the prediction of $q = 3.50$ in the classical model of a collisional cascade presented by Dohnanyi (1969) and to recent numerical results by Löhne et al. (2012), Schüppler et al. (2014), and Schüppler et al. (2015) for specific debris disk systems. The models of Pan & Schlichting (2012) that incorporate size-dependent velocity distributions where velocity decreases with decreasing particle size produce significantly steeper size distributions. Numerical models by Gáspár et al. (2012) yield some q values consistent with these results, but only by increasing the scaling of the strength curve in excess of fiducial values. Shallower size distributions can be produced by models that allow for a velocity distribution where velocity increases with decreasing particle size or models that consider colliding bodies not dominated by material strength.
2. Although limited by small number statistics, the observations suggest a trend in q as a function of stellar type. The weighted mean for stars with spectral types A–F is 3.45 ± 0.02 and 3.30 ± 0.03 for spectral types G–M. We see no evidence for trends in q as a function of system age or gas abundance in the disk.
3. Introducing a cutoff in the grain size distribution at small sizes due to radiation pressure can superimpose waves on the power law grain distribution. We examine a range of analytic models varying the blowout size (a_{bl}), the relative collision velocity (v_{rel}), and the collision energy (Q_D^*). Changing the blowout size from $1 \mu\text{m}$ (typical for K and M stars) to $10 \mu\text{m}$ (for A and B stars) produces measurable waves in the grain size

distribution and the resulting dust opacity. For a reasonable range of parameter values, the waves produced vary the inferred dust opacity power law index β between 0.5 and 1.1, a spread in values comparable to the scatter in the observations. In realistic debris disk systems, however, inhomogeneities in densities and fragmentation energies likely weaken or smear these modulations.

4. The VLA observations of the AU Mic system show significant and variable emission from stellar activity at centimeter wavelengths on timescales from minutes to months. Given this new evidence, the asteroid belt posited by MacGregor et al. (2013) is not needed to explain any aspects of the observed millimeter emission. High angular resolution at centimeter wavelengths allows us to distinguish this stellar emission from the dust disk emission. However, the vast majority of debris disks in the sample have not been resolved at centimeter wavelengths. Given this, we are unable to separate disk dust emission from any stellar contamination (or extragalactic background contamination), if present, for these systems. Higher resolution observations at millimeter and centimeter wavelengths are needed to place better constraints on the contribution of stellar activity to the total flux measurements.

These VLA and ATCA observations provide the longest wavelength flux measurements of these fifteen debris disk systems to date. But, observations at centimeter wavelengths of new systems are needed to continue to grow the sample and place better constraints on any trends in the grain size distribution with stellar or disk properties.

M.A.M acknowledges support from a National Science Foundation Graduate Research Fellowship (DGE1144152). The National Radio Astronomy Observatory is a facility of the National Science Foundation operated under cooperative agreement by Associated Universities, Inc. The Australia Telescope Compact Array is part of the Australia Telescope National Facility which is funded by the Australian Government for operation as a National Facility managed by CSIRO. We thank Margaret Pan, Hilke Schlichting, and Scott Kenyon for helpful conversations. We thank Meredith Hughes, Kate Su, David Rodriguez, Sebastián Marino, Aaron Boley, and Jacob White for providing data prior to publication. We also thank the anonymous referee for a careful and thoughtful review.

REFERENCES

- Apai, D., Janson, M., Moro-Martín, A., et al. 2008, *ApJ*, 672, 1196
- Ardila, D. R., Golimowski, D. A., Krist, J. E., et al. 2004, *ApJ*, 617, L147

- Asphaug, E., & Benz, W. 1996, *Icarus*, 121, 225
- Backman, D. E., & Paresce, F. 1993, in *Protostars and Planets III*, ed. E. H. Levy & J. I. Lunine, 1253–1304
- Benz, W., & Asphaug, E. 1999, *Icarus*, 142, 5
- Biller, B. A., Liu, M. C., Rice, K., et al. 2015, *MNRAS*, 450, 4446
- Binks, A. S., & Jeffries, R. D. 2014, *MNRAS*, 438, L11
- Boley, A. C., Payne, M. J., Corder, S., et al. 2012, *ApJ*, 750, L21
- Brittain, S. D., & Rettig, T. W. 2002, *Nature*, 418, 57
- Butler, R. P., Wright, J. T., Marcy, G. W., et al. 2006, *ApJ*, 646, 505
- Campo Bagatin, A., Cellino, A., Davis, D. R., Farinella, P., & Paolicchi, P. 1994, *Planet. Space Sci.*, 42, 1079
- Carpenter, J. M., Wolf, S., Schreyer, K., Launhardt, R., & Henning, T. 2005, *AJ*, 129, 1049
- Choquet, É., Perrin, M. D., Chen, C. H., et al. 2015, *ArXiv e-prints*, arXiv:1512.02220
- Clampin, M., Krist, J. E., Ardila, D. R., et al. 2003, *AJ*, 126, 385
- Cranmer, S. R., Wilner, D. J., & MacGregor, M. A. 2013, *ApJ*, 772, 149
- Czekala, I., Andrews, S. M., Jensen, E. L. N., et al. 2015, *ApJ*, 806, 154
- D’Alessio, P., Calvet, N., & Hartmann, L. 2001, *ApJ*, 553, 321
- Debes, J. H., Weinberger, A. J., & Song, I. 2008, *ApJ*, 684, L41
- Dent, W. R. F., Greaves, J. S., & Coulson, I. M. 2005, *MNRAS*, 359, 663
- Dent, W. R. F., Wyatt, M. C., Roberge, A., et al. 2014, *Science*, 343, 1490
- Desidera, S., Covino, E., Messina, S., et al. 2011, *A&A*, 529, A54
- Dohnanyi, J. S. 1969, *J. Geophys. Res.*, 74, 2531
- Draine, B. T. 2006, *ApJ*, 636, 1114
- Dullemond, C. P., & Dominik, C. 2004, *A&A*, 417, 159

- Fletcher, L., Cargill, P. J., Antiochos, S. K., & Gudiksen, B. V. 2015, *Space Sci. Rev.*, 188, 211
- France, K., Parke Loyd, R. O., & Brown, A. 2015, *IAU General Assembly*, 22, 28599
- Gáspár, A., Psaltis, D., Rieke, G. H., & Özel, F. 2012, *ApJ*, 754, 74
- Geers, V. C., Gorti, U., Meyer, M. R., et al. 2012, *ApJ*, 755, 8
- Goto, M., Usuda, T., Dullemond, C. P., et al. 2006, *ApJ*, 652, 758
- Graham, J. R., Kalas, P. G., & Matthews, B. C. 2007, *ApJ*, 654, 595
- Greaves, J. S., Hales, A. S., Mason, B. S., & Matthews, B. C. 2012, *MNRAS*, 423, L70
- Greaves, J. S., Sibthorpe, B., Acke, B., et al. 2014, *ApJ*, 791, L11
- Heap, S. R., Lindler, D. J., Lanz, T. M., et al. 2000, *ApJ*, 539, 435
- Hines, D. C., Schneider, G., Hollenbach, D., et al. 2007, *ApJ*, 671, L165
- Housen, K. R., & Holsapple, K. A. 1999, *Icarus*, 142, 21
- Hughes, A. M., Wilner, D. J., Kamp, I., & Hogerheijde, M. R. 2008, *ApJ*, 681, 626
- Jewitt, D. C., & Sheppard, S. S. 2002, *AJ*, 123, 2110
- Kalas, P., Fitzgerald, M. P., & Graham, J. R. 2007, *ApJ*, 661, L85
- Kalas, P., Graham, J. R., & Clampin, M. 2005, *Nature*, 435, 1067
- Kalas, P., Liu, M. C., & Matthews, B. C. 2004, *Science*, 303, 1990
- Kenyon, S. J., & Bromley, B. C. 2002, *ApJ*, 577, L35
- . 2008, *ApJS*, 179, 451
- . 2016, *ApJ*, 817, 51
- Krivov, A. V. 2007, *Dust in Planetary Systems*, 643, 123
- Krivov, A. V., Löhne, T., & Sremčević, M. 2006, *A&A*, 455, 509
- Krivov, A. V., Eiroa, C., Löhne, T., et al. 2013, *ApJ*, 772, 32
- Leto, G., Pagano, I., Linsky, J. L., Rodonò, M., & Umana, G. 2000, *A&A*, 359, 1035

- Liseau, R., Risacher, C., Brandeker, A., et al. 2008, *A&A*, 480, L47
- Liseau, R., Eiroa, C., Fedele, D., et al. 2010, *A&A*, 518, L132
- Liseau, R., Vlemmings, W., Bayo, A., et al. 2015, *A&A*, 573, L4
- Löhne, T., Augereau, J.-C., Ertel, S., et al. 2012, *A&A*, 537, A110
- MacGregor, M. A., Wilner, D. J., Andrews, S. M., & Hughes, A. M. 2015a, *ApJ*, 801, 59
- MacGregor, M. A., Wilner, D. J., Andrews, S. M., Lestrade, J.-F., & Maddison, S. 2015b, *ApJ*, 809, 47
- MacGregor, M. A., Wilner, D. J., Rosenfeld, K. A., et al. 2013, *ApJ*, 762, L21
- Maehara, H., Shibayama, T., Notsu, Y., et al. 2015, *Earth, Planets, and Space*, 67, 59
- Mamajek, E. E. 2012, *ApJ*, 754, L20
- Mamajek, E. E., & Hillenbrand, L. A. 2008, *ApJ*, 687, 1264
- Maness, H. L., Kalas, P., Peek, K. M. G., et al. 2009, *ApJ*, 707, 1098
- Matthews, B. C., Krivov, A. V., Wyatt, M. C., Bryden, G., & Eiroa, C. 2014, *Protostars and Planets VI*, 521
- Mazoyer, J., Boccaletti, A., Augereau, J.-C., et al. 2014, *ArXiv e-prints*, arXiv:1409.0710
- Meshkat, T., Bailey, V., Rameau, J., et al. 2013, *ApJ*, 775, L40
- Mitra-Kraev, U., Harra, L. K., Güdel, M., et al. 2005, *A&A*, 431, 679
- Moór, A., Pascucci, I., Kóspál, Á., et al. 2011, *ApJS*, 193, 4
- Morales, F. Y., Bryden, G., Werner, M. W., & Stapelfeldt, K. R. 2013, *ApJ*, 776, 111
- Morales, F. Y., Rieke, G. H., Werner, M. W., et al. 2011, *ApJ*, 730, L29
- Mouillet, D., Lagrange, A. M., Augereau, J. C., & Ménard, F. 2001, *A&A*, 372, L61
- Mustill, A. J., & Wyatt, M. C. 2009, *MNRAS*, 399, 1403
- Najita, J., & Williams, J. P. 2005, *ApJ*, 635, 625
- Nilsson, R., Liseau, R., Brandeker, A., et al. 2010, *A&A*, 518, A40
- Nordström, B., Mayor, M., Andersen, J., et al. 2004, *A&A*, 418, 989

- Osman, K. T., Matthaeus, W. H., Greco, A., & Servidio, S. 2011, *ApJ*, 727, L11
- Pan, M., & Sari, R. 2005, *Icarus*, 173, 342
- Pan, M., & Schlichting, H. E. 2012, *ApJ*, 747, 113
- Panić, O., Holland, W. S., Wyatt, M. C., et al. 2013, *MNRAS*, 435, 1037
- Pawellek, N., & Krivov, A. V. 2015, *MNRAS*, 454, 3207
- Pawellek, N., Krivov, A. V., Marshall, J. P., et al. 2014, *ApJ*, 792, 65
- Pecaut, M. J., Mamajek, E. E., & Bubar, E. J. 2012, *ApJ*, 746, 154
- Reidemeister, M., Krivov, A. V., Stark, C. C., et al. 2011, *A&A*, 527, A57
- Ricarte, A., Moldvai, N., Hughes, A. M., et al. 2013, *ApJ*, 774, 80
- Ricci, L., Carpenter, J. M., Fu, B., et al. 2015a, *ApJ*, 798, 124
- Ricci, L., Maddison, S. T., Wilner, D., et al. 2015b, *ApJ*, 813, 138
- Ricci, L., Testi, L., Maddison, S. T., & Wilner, D. J. 2012, *A&A*, 539, L6
- Ricci, L., Testi, L., Natta, A., & Brooks, K. J. 2010a, *A&A*, 521, A66
- Ricci, L., Testi, L., Natta, A., et al. 2010b, *A&A*, 512, A15
- Roberge, A., Kamp, I., Montesinos, B., et al. 2013, *ApJ*, 771, 69
- Robinson, R. D., Linsky, J. L., Woodgate, B. E., & Timothy, J. G. 2001, *ApJ*, 554, 368
- Roccatagliata, V., Henning, T., Wolf, S., et al. 2009, *A&A*, 497, 409
- Rodigas, T. J., Hinz, P. M., Leisenring, J., et al. 2012, *ApJ*, 752, 57
- Schneider, G., Silverstone, M. D., Hines, D. C., et al. 2006, *ApJ*, 650, 414
- Schneider, G., Grady, C. A., Hines, D. C., et al. 2014, *ArXiv e-prints*, arXiv:1406.7303
- Schneider, P. C., & Schmitt, J. H. M. M. 2010, *A&A*, 516, A8
- Schüppler, C., Löhne, T., Krivov, A. V., et al. 2014, *A&A*, 567, A127
- . 2015, *A&A*, 581, A97
- Silverstone, M. D. 2000, PhD thesis, UNIVERSITY OF CALIFORNIA, LOS ANGELES

- Smith, K., Güdel, M., & Audard, M. 2005, *A&A*, 436, 241
- Stark, C. C., Schneider, G., Weinberger, A. J., et al. 2014, *ApJ*, 789, 58
- Steele, A., Hughes, A. M., Carpenter, J., et al. 2016, *ApJ*, 816, 27
- Su, K. Y. L., Morrison, S., Malhotra, R., et al. 2015, *ApJ*, 799, 146
- Thébault, P., & Augereau, J.-C. 2007, *A&A*, 472, 169
- Thébault, P., Augereau, J. C., & Beust, H. 2003, *A&A*, 408, 775
- Thébault, P., & Wu, Y. 2008, *A&A*, 481, 713
- Thi, W.-F., Pinte, C., Pantin, E., et al. 2014, *A&A*, 561, A50
- Torres, C. A. O., Quast, G. R., Melo, C. H. F., & Sterzik, M. F. 2008, *Young Nearby Loose Associations*, ed. B. Reipurth, 757
- van Leeuwen, F. 2007, *A&A*, 474, 653
- Velli, M., Pucci, F., Rappazzo, F., & Tenerani, A. 2015, *Philosophical Transactions of the Royal Society of London Series A*, 373, 40262
- Vitense, C., Krivov, A. V., Kobayashi, H., & Löhne, T. 2012, *A&A*, 540, A30
- Wahhaj, Z., Koerner, D. W., & Sargent, A. I. 2007, *ApJ*, 661, 368
- Weinberger, A. J., Rich, R. M., Becklin, E. E., Zuckerman, B., & Matthews, K. 2000, *ApJ*, 544, 937
- White, S. M., Lim, J., & Kundu, M. R. 1994, *ApJ*, 422, 293
- Wichmann, R., Schmitt, J. H. M. M., & Hubrig, S. 2003, *A&A*, 399, 983
- Wyatt, M. C. 2008, *ARA&A*, 46, 339
- Wyatt, M. C., Clarke, C. J., & Booth, M. 2011, *Celestial Mechanics and Dynamical Astronomy*, 111, 1
- Zuckerman, B., Forveille, T., & Kastner, J. H. 1995, *Nature*, 373, 494

A. Radio Light Curves of AU Mic

AU Mic is an active M dwarf star that is known to exhibit radio-wave bursts. In quiescence, previous observations placed upper limits on the flux at radio wavelengths, $< 120 \mu\text{Jy}$ at 3.6 cm (White et al. 1994; Leto et al. 2000). Recent ALMA observations of the system at 1.3 mm revealed a compact central emission peak with a flux of $\sim 320 \mu\text{Jy}$ in addition to the continuum dust emission from the debris belt and greatly in excess of the expected photospheric flux at this long wavelength. Cranmer et al. (2013) model this excess emission as arising from a hot stellar corona. Schüppler et al. (2015) suggest that chromospheric emission from the star could also contribute at millimeter and radio wavelengths.

These new VLA observations of AU Mic offer a unique glimpse at the variations in radio emission from the star on minute to month-long timescales. Observations were taken at 9 mm (Ka band) in the DnC configuration on May 9 and 11, 2013 and in the C configuration on June 21, 2013. Each of the three scheduling blocks (SBs) was a total of 105 minutes in length. Observations of AU Mic were interleaved with the gain calibrator, J2101-2933, in a 4 minute cycle, with 3 minutes on-source.

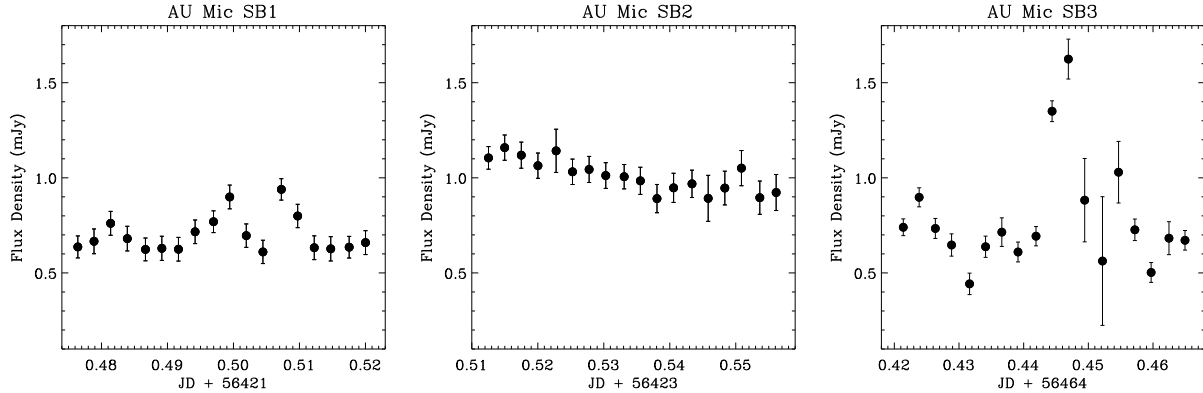


Fig. 5.— Stellar light curves for AU Mic showing the variation in flux density over the course of our three observations. The flux density was determined for each 3 minute integration using the CASA task `uvmodelfit` to fit a point source model to the visibilities.

Figure 5 shows the stellar light curves for each of the three SBs. To determine the flux density, we used the CASA task `uvmodelfit` to fit a point source model to the visibilities from each 3 minute on-source integration. There is strong radio emission from the star present in all 3 SBs with a flux of $0.5 - 1.5 \text{ mJy}$. During the third SB, the star appears to have flared strongly, increasing in brightness by $100 - 150\%$.

Cranmer et al. (2013) simulated the time-steady coronal emission of AU Mic in both X-ray and millimeter bands, but they did not account for time variability. In order to begin

to estimate the relative enhancements in the coronal emission during flare times, we re-ran the Cranmer et al. (2013) model for a range of imposed variations in the coronal heating. We assumed that a fractional filling factor, f , of the coronal volume was occupied by flare-like plasma, and that the photospheric driving velocity, v_{\perp} , of MHD turbulence was enhanced by a dimensionless factor, ξ , in that region. Thus, for a range of input parameters ($f \leq 1$, $\xi \geq 1$) we simulated both the total X-ray luminosity, L_X , and the thermal free-free emission, I_{ν} , at the observed VLA wavelength of 9 mm. The goal was to find a combination of plausible f and ξ values that would produce a relative enhancement in L_X of order 30% to 60% (to match the flare amplitudes reported by Smith et al. 2005; Mitra-Kraev et al. 2005; Schneider & Schmitt 2010) simultaneously with an increase in the 9 mm continuum of order 100 – 150% (see Figure 5).

To match the observed ranges of flux density enhancement, we found that the filling factor f must be larger than 0.48, and the boundary velocity enhancement factor ξ must be within the range of 4.1 – 8.2. These values of ξ correspond to an increase in the total nonthermal energy input of order 20 – 70 in the flare regions. The maximum enhanced temperature in this subset of models was found to be about 13 MK. This is reminiscent of the hottest of the three temperature components (3.37, 7.78, and 17.3 MK) inferred from *Chandra* spectra of AU Mic by Schneider & Schmitt (2010). The quiescent model of Cranmer et al. (2013) successfully predicted temperatures between the two lower *Chandra* values, but the largest value appeared to be explainable only by flare activity.

A better understanding of cool-star flare activity will depend on broader observational coverage in both time and wavelength. *Kepler* has opened up new vistas of study of how properties of white-light “superflares” on active stars may relate to the more familiar case of the Sun (Maehara et al. 2015). However, recent multi-wavelength surveys of M and K dwarf exoplanet host stars (e.g., France et al. 2015) are also revealing new information about weak flares that do not manifest at visible wavelengths. For the better-resolved case of the Sun, recent observations and simulations show that nearly *all* coronal heating activity may take the form of a distribution of flare events with a range of strengths and timescales (Fletcher et al. 2015). Even models that invoke MHD waves and turbulence appear to require the spontaneous production of nanoflare-like magnetic reconnection events as a final product of the cascade from large to small eddies (e.g., Osman et al. 2011; Velli et al. 2015).

Table 1. Debris Disk Sample Characteristics

Source	α (J2000)	δ (J2000)	Spectral Type	L_* [L_\odot]	d ^a [pc]	Age [Myr]	PA ^b [°]	Disk gas?
HD 377	00 08 25.8	+06 37 00.5	G2	1.0	30	150	47	N
49 Ceti	01 34 37.8	−15 40 34.9	A1	20.	59	40	101	Y
HD 15115	02 26 16.3	+06 17 33.1	F2	3.3	45	21	279	N
HD 61005	07 35 47.5	−32 12 14.0	G8	0.5	35	40	70	N
HD 104860	12 04 33.7	+66 20 11.7	F8	1.4	48	140	1	N
HD 141569	15 49 57.8	−03 55 16.2	B9.5	21.	116	5	356	Y
AU Mic	20 45 09.8	−31 20 31.8	M1	0.1	10	21	128	N
q ¹ Eri	01 42 29.3	−53 44 27.0	F9	1.2	17	4800	55	N
ϵ Eri	03 32 54.9	−09 27 29.4	K2	0.3	3	400 – 800	0	N
β Pic	05 47 17.1	−51 03 59.4	A6	8.7	19	21	32	Y
HD 95086	10 57 03.0	−68 40 02.5	A8	8.6	90	17	15	N
HD 107146	12 19 06.5	+16 32 53.9	G2	1.0	29	80 – 200	148	N
AK Sco	16 54 44.8	−36 53 18.6	F5	3.0	142	18	49	Y
HD 181327	19 22 58.9	−54 32 17.0	F6	3.3	51	12	107	N
Fomalhaut	22 57 39.0	−29 37 20.1	A4	16.	7	440	156	N

Note. — ^a All distances measured by van Leeuwen (2007)

^b Position angle measured east of north to the disk major axis

References for stellar and disk properties: HD 377, Geers et al. (2012), Choquet et al. (2015); 49 Ceti, Torres et al. (2008), Hughes et al. (2008); HD 15115, Binks & Jeffries (2014), Kalas et al. (2007); HD 61005, Desidera et al. (2011), Hines et al. (2007); HD 104860, Steele et al. (2016); HD 141569, Weinberger et al. (2000), White et al. (in prep.); AU Mic, Binks & Jeffries (2014), MacGregor et al. (2013); q¹ Eri, Butler et al. (2006), Liseau et al. (2008), Liseau et al. (2010); ϵ Eri, Mamajek & Hillenbrand (2008), Greaves et al. (2014); β Pic, Binks & Jeffries (2014), Dent et al. (2014), Heap et al. (2000); HD 95086, Meshkat et al. (2013), Su et al. (2015); HD 107146, Wichmann et al. (2003), Ardila et al. (2004); AK Sco, Pecaut et al. (2012), Czekala et al. (2015); HD 181327, Nordström et al. (2004), Schneider et al. (2006); Fomalhaut, Mamajek (2012), Kalas et al. (2005)

Table 2. VLA Observations

Source	Obs. Dates	Config.	Ant.	Baseline Lengths [km]	API ^a rms [°]	On-source time [min]	Gain calibrator(s)
HD 377	2014 Jul 3	D	27	0.04 – 1.31	6.6	64.8	J0011+0823
	2014 Jul 10	D	26	0.04 – 1.31	5.6	62.1	
49 Ceti	2014 Jul 13	D	27	0.04 – 1.31	5.8	63.3	J0132–1654
	2014 Jul 14	D	25	0.04 – 1.31	3.4	66.4	
HD 15115	2014 Jul 8	D	26	0.04 – 1.31	3.0	65.7	J0224+0659
	2014 Jul 11	D	26	0.04 – 1.31	3.1	65.6	
HD 61005	2014 Sep 19	DnC	27	0.04 – 2.11	1.5	62.0	J0747–3310
	2014 Sep 20	DnC	27	0.04 – 2.11	3.3	62.2	
HD 104860	2014 Aug 30	D	27	0.04 – 1.31	5.3	61.4	J1220+7105
	2014 Aug 30	D	27	0.04 – 1.31	4.6	61.2	
HD 141569	2014 Jun 6	D	25	0.04 – 1.31	4.0	61.5	J1557–0001
AU Mic	2013 May 9	DnC	27	0.04 – 2.11	4.1	49.7	J2101–2933
	2013 May 11	DnC	27	0.04 – 2.11	2.8	49.9	
	2013 Jun 21	C	27	0.05 – 3.38	1.3	50.0	

Note. — ^a Measure of the tropospheric contribution to the interferometric phase determined by the Atmospheric Phase Interferometer (API), an interferometer comprised of two 1.5-m antennas separated by 300 m, observing an 11.7 GHz beacon from a geostationary satellite.

Table 3. Results of the VLA Observations

Source	Beam Size ^a [″]	Beam P.A. ^b [deg.]	$F_{9\text{mm}}$ [μJy]	rms Noise [μJy/beam]
HD 377	2.8×2.4	21.2	< 13.1	4.4
49 Ceti	3.8×2.6	339.6	25.1	5.5
HD 15115	3.0×2.4	314.0	12.8	4.1
HD 61005	2.6×2.0	45.6	57.3	8.6
HD 104860	3.1×2.3	75.6	14.0	3.5
HD 141569	3.0×2.4	338.6	85.0	5.1
AU Mic	3.1×2.8	41.0	> 60.8	5.2

Note. — ^a Beam size determined with natural weighting

^b Beam position angle measured from east of north

Table 4. Grain Size Distribution Slopes (q)

Source	(Sub)mm λ [mm]	(Sub)mm Instr.	F_{mm} [mJy]	Ref. ^a	α_{mm}	R_{dust}^b [AU]	Ref. ^a	T_{dust}^c [K]	α_{Pl}	q
HD 377	0.87	SMA	3.5 ± 1.0	1	> 2.39	50	1	44	1.92 ± 0.02	> 3.26
49 Ceti	0.85	ALMA	17 ± 3	2	2.76 ± 0.11	120	2	55	1.94 ± 0.01	3.46 ± 0.08
HD 15115	1.3	SMA	2.6 ± 0.6	3	2.75 ± 0.15	110	15	45	1.92 ± 0.02	3.46 ± 0.10
HD 61005	1.3	SMA	7.2 ± 0.3	4	2.49 ± 0.08	70	4	30	1.91 ± 0.03	3.32 ± 0.06
HD 104860	1.3	SMA	4.4 ± 1.1	1	3.08 ± 0.23	110	1	28	$1.90^{+0.02}_{-0.04}$	3.64 ± 0.15
HD 141569	0.87	ALMA	3.78 ± 0.45	5	1.63 ± 0.06	30	5	109	1.97 ± 0.02	2.84 ± 0.05
AU Mic	1.3	ALMA	7.14 ± 0.15	6	< 2.46	20	6	25	$1.90^{+0.03}_{-0.07}$	< 3.31
q ¹ Eri	0.87	APEX	39.4 ± 4.1	7	2.94 ± 0.10	85	7	33	$1.88^{+0.02}_{-0.04}$	3.59 ± 0.08
ϵ Eri	1.3	SMA	17.2 ± 5.0	8	> 2.39	64	8	27	$1.89^{+0.03}_{-0.06}$	> 3.28
β Pic	0.87	ALMA	60 ± 6	9	2.81 ± 0.10	85	9	52	1.93 ± 0.01	3.49 ± 0.08
HD 95086	1.3	ALMA	3.1 ± 0.18	10	2.37 ± 0.15	90	16	50	1.93 ± 0.01	3.24 ± 0.10
HD 107146	1.25	ALMA	12.5 ± 1.3	11	2.55 ± 0.11	60	11	30	$1.90^{+0.05}_{-0.02}$	3.36 ± 0.07
AK Sco	1.3	ALMA	32.65 ± 0.07	12	2.62 ± 0.03	14	12	95	1.97 ± 0.01	3.36 ± 0.04
HD 181327	1.3	ALMA	7.5 ± 0.1	13	2.38 ± 0.05	90	17	60	1.94 ± 0.01	3.24 ± 0.05
Fomalhaut	0.85	SCUBA	27.0 ± 3.0	14	2.70 ± 0.17	135	18	48	1.91 ± 0.02	3.44 ± 0.11

Note. — ^a References: 1) Steele et al. (2016), 2) Hughes et al. (in prep), 3) MacGregor et al. (2015a), 4) Ricarte et al. (2013), 5) White et al. (in prep), 6) MacGregor et al. (2013), 7) Liseau et al. (2008), 8) MacGregor et al. (2015b), 9) Dent et al. (2014), 10) Su et al. (2016, in prep), 11) Ricci et al. (2015a), 12) Czekala et al. (2015), 13) Marino et al. (in prep), 14) Ricci et al. (2012), 15) MacGregor et al. (2015a), 16) Su et al. (2015), 17) Stark et al. (2014), 18) Boley et al. (2012)

^b Uncertainty on R_{dust} assumed to be 20%

^c Uncertainty on T_{dust} assumed to be 10%